Available online at www.sciencedirect.com
ScienceDirect
Trans. Nonferrous Met. Soc. China 32(2022) 947−956
Transactions of Nonferrous Metals Society of China
www.tnmsc.cn

# Effect of partial recrystallization on microstructure and tensile properties of NiFeCoCrMn high-entropy alloy

Hui DU[1,2,3,4], Jia-hong CAI[1,2], Ya-song WANG[4], Jun-qing YAO[4], Qiang CHEN[5], Yu CUI[1,2], Xin-wang LIU[4]

1. Key Laboratory of Metallurgical Equipment and Control Technology, Ministry of Education, Wuhan University of Science and Technology, Wuhan 430081, China;
2. Hubei Key Laboratory of Mechanical Transmission and Manufacturing Engineering, Wuhan University of Science and Technology, Wuhan 430081, China;
3. Precision Manufacturing Institute, Wuhan University of Science and Technology, Wuhan 430081, China;
4. State Key Laboratory of Materials Processing and Die & Mould Technology, School of Materials Science and Engineering, Huazhong University of Science and Technology, Wuhan 430074, China;
5. Southwest Technology and Engineering Research Institute, Chongqing 400039, China

Received 28 March 2021; accepted 1 November 2021

**Abstract:** To obtain a balance between strength and ductility in NiFeCoCrMn high-entropy alloy, the degree of dislocation strengthening was tuned via partial recrystallization during traditional thermomechanical processing (cold rolling and recrystallization). The tensile properties in each state were then examined. Significant improvements in uniform elongation and work hardening rate, with decrease in yield strength and ultimate tensile strength, are associated with increase in the recrystallized fraction, i.e., reductions in the degree of strain hardening. In particular, recrystallized fractions of 37% and 74% are obtained by annealing at 650 °C for 10 min and 15 min, respectively, which results in yield strengths of 1003 MPa and 742 MPa and uniform elongations of 4% and 24%, respectively. The strengthening is due to the unrecrystallized grains with a high density of dislocations, whereas the ductility benefits from the presence of recrystallized strain-free grains.

**Key words:** high-entropy alloy; partial recrystallization; microstructure; tensile property; strengthening mechanism

## 1 Introduction

High-entropy alloys (HEAs) containing four or more elements in equiatomic concentrations are referred to as multi-principal-element alloys and have received significant attention in recent years [1−5]. The equiatomic NiFeCoCrMn high-entropy alloy with a face-centered cubic (FCC) structure was first reported by CANTOR et al [6] and has attracted extensive attention recently due to its excellent ductility and fracture toughness at room and cryogenic temperatures [7−16]. It has, therefore, been considered as a base for the development of engineering applications.

Although the NiFeCoCrMn HEA has good ductility in a wide temperature range, its room-temperature strength is insufficient for engineering applications. Thus, it is critical to incorporate strengthening mechanisms in this alloy; extensive research has been conducted into well-known mechanisms, such as solid solution, grain boundary, dislocation, and second-phase strengthening. For example, HE et al [17] added Al to the NiFeCoCrMn HEA and produced both solid solution strengthening at low Al concentrations and body-centered-cubic (BCC) second-phase strengthening at high Al concentrations. The results

**Corresponding author:** Qiang CHEN, Tel: +86-23-68792286, E-mail: 2009chenqiang@hfut.edu.cn;
Xin-wang LIU, Tel: +86-27-87543776, E-mail: liuxw@hust.edu.cn
DOI: 10.1016/S1003-6326(22)65841-2

indicate that the strengthening provided by the solid solution of Al is relatively slight, while the second-phase precipitation strengthening is remarkable. Other efforts have been attempted to significantly enhance the strength of this HEA by modifying the second-phase precipitations. The nano-sized $L1_2$ and $D0_{22}$ precipitations have been proven to be effective in providing extraordinary hardening [18−20]. Nevertheless, elaborate compositional design and complex heat treatment procedures are generally required to obtain the desired hardening with these strengthening methods. In contrast, dislocation strain hardening is a simple and effective approach with an easy process; it only requires cold deformation and a certain degree of annealing. For instance, dislocation strengthening in Al-containing NiFeCoCrMn HEAs has been reported by XU et al [21], who suggested that early small strain produces low-density dislocation arrays and bowed dislocations in FCC grains, while the dislocation climb and shearing mechanisms dominate inside BCC grains. BAE et al [22] cold-rolled and recrystallized NiFeCoCrMn HEAs for 1 h at various temperatures from 650 to 1000 °C and found that a trade-off between mechanical properties and stretch formability could be achieved by partial recrystallization. Some other works have also explored partial recrystallization of HEAs; however, they have either focused on $CrFeCoNiAl_{0.1}$ HEA or the carbon effect and cryogenic-temperature properties, but not on the recrystallization fraction adjustment of NiFeCoCrMn HEA [23−28]. There is a lack of research on specific adjustment of the recrystallization fraction to achieve a balance between strength and ductility in NiFeCoCrMn HEA. The NiFeCoCrMn HEA has many unique properties and is worth revisiting to determine the optimal balance between strength and ductility via simple partial recrystallization using traditional room-temperature cold rolling and annealing.

In the present study, NiFeCoCrMn HEA microstructures with various degrees of dislocation strain hardening were formed by conventional cold rolling and partial recrystallization. Quasi-static tensile tests of four different recrystallized fractions (0%, 37%, 74% and 100 %) at room temperature were conducted. Furthermore, related mechanisms of strengthening and toughening are discussed.

## 2 Experimental

The NiFeCoCrMn ingots were prepared by arc-melting a mixture of pure metals (purity >99.9 wt.%) except Mn (>99 wt.%) in a high-purity argon atmosphere. An additional of 1 wt.% Mn was added to compensate for its evaporation similar to the previous work [29,30]. After the raw materials were loaded in the arc melter, the chamber was first evacuated to ~$5\times10^{-2}$ Pa, backfilled with pure Ar, then evacuated twice to dilute the residual air inside the chamber, and finally backfilled to a pressure of ~$5\times10^{4}$ Pa. Before the materials were melted, a small piece of pure Ti was melted to getter any residual air that might be present in the chamber. The buttons were remelted and flipped five times to ensure chemical homogeneity before they were drop-cast into a rectangular copper mold with the dimensions of 10 mm × 17 mm × 70 mm. After solidification, the ingots were cleaned and dried, encapsulated in evacuated quartz tubes, and homogenized for 48 h at 1200 °C to minimize any casting-related segregation. Then, the homogenized samples were cold-rolled along the longitudinal ingot direction to sheets with a final thickness of ~1.2 mm, corresponding to a reduction in thickness of ~88%. The rolled sheets were annealed for 10 and 15 min at 650 °C and for 10 min at 800 °C to obtain partially and fully recrystallized microstructures (referred to as as-rolled, H650-10, H650-15 and H800-10 samples, respectively, afterwards).

Phases present in the alloys were identified by X-ray diffraction (XRD) using a SHIMADZU XRD−7000S diffractometer (Cu $K_\alpha$ target, $\lambda$= 0.154 nm, voltage 40 kV, $2\theta$ range from 20° to 90°, and scanning speed 3 (°)/min). Microstructures were analyzed by electron back-scatter diffraction (EBSD) with a field emission scanning electron microscope (Zeiss GeminiSEM 300) on the cross sections of samples and the data were interpreted using an HKL Channel5 analysis software. The recrystallized fraction was characterized by EBSD which has been a widely-adopted method for this aim [31]. The microstructures were also examined by using a Nova 400 NanoSEM scanning electron microscopy (SEM) equipped with an energy dispersive X-ray spectroscopy (EDX). Specimens were ground with SiC paper to a grit size of 7 μm

and then electrochemically polished using Struers LectroPol−5 for 10 s in a mixture of 10 vol.% perchloric acid and 90 vol.% ethanol at room temperature and an applied voltage of 40 V.

Flat dog-bone-shaped specimens (gage length 12 mm, gage width 2.5 mm, and thickness ~1.2 mm) were cut by electrical discharge machining (EDM) from the sheets and ground through 1000-grit SiC paper. The tensile tests were performed using a SHIMADZU AG−100 kN testing machine at an engineering strain rate of $1\times10^{-3}$ $s^{-1}$ in air at room temperature.

## 3 Results and discussion

### 3.1 Microstructures

The XRD analysis of the four HEAs with different recrystallized fractions (as shown in Fig. 1) shows peaks corresponding to the FCC structure, which is consistent with other reports [32]. Since phases with a low volume fraction or with the same crystallographic structure and a slightly different lattice parameter cannot be differentiated by XRD, further analysis is needed. The diffraction peaks shift according to different recrystallized fractions. It has been found in other alloys that cold working can lead to a change in the lattice parameter that is reflected by a shift in the XRD diffraction peaks [33,34]. Deformation introduces changes in the internal structure within the grains, causing the formation of substructures (domains) and leading to broadening of the diffraction peaks of the deformed alloys. During cold rolling, a large number of dislocations are introduced into the material but they are not randomly distributed. These dislocations are accommodated in a variety of ways, including creation of internal boundaries.

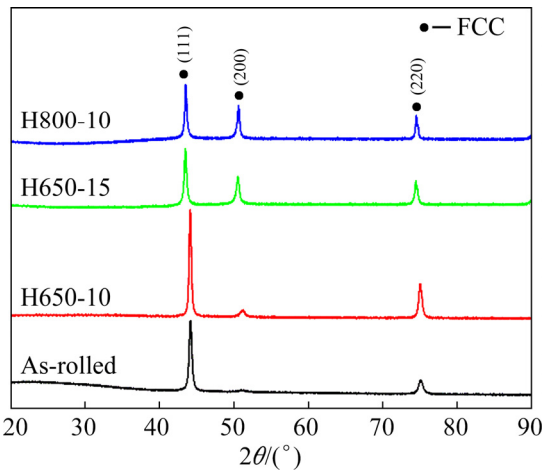


**Fig. 1** XRD patterns of as-rolled, H650-10, H650-15 and H800-10 specimens of NiFeCoCrMn HEAs

The microstructures of the NiFeCoCrMn HEAs after cold rolling and recrystallization annealing are strongly temperature- and time-dependent on the annealing parameters. Figure 2 shows EBSD inverse pole figure (IPF) maps of the as-rolled and annealed samples. Cold rolling induces a large amount of plastic deformation and the grains become elongated along the rolling direction. It is known that the deformed microstructure includes a high density of dislocations and even deformation twins in the grain interior in alloys with low stacking fault energy [35]. Although EBSD cannot detect deformation twins clearly, the existence of deformation twins in the NiFeCoCrMn HEA during room-temperature cold rolling has been proven previously [22]. This is ascribed to the fact that the stress level during cold rolling reaches the critical resolved shear stress for twinning onset [36]. A typical FCC rolling texture is also detected and the details are described in Ref. [22]. The microstructure of Sample H650-10 is composed of recrystallized equiaxed grains with a recrystallized fraction ($f_{rec}$) of ~37%, with the rest deformed microstructure. The average grain size of the equiaxed grains is ~1.1 μm. Recrystallization occurs nonuniformly, as evidenced by equiaxed grains distributed in certain regions. This is related to the varied storage energy in the grains during the cold rolling process, which is the driving force of recrystallization [37]. By prolonging the duration to 15 min at 650 °C, the $f_{rec}$ is significantly increased to ~74% and the average size of equiaxed grains increases slightly to ~1.3 μm. It should be noted that the EBSD analysis shows the sigma phase in both H650-10 and H650-15 HEAs with fractions ≤0.4%, as indicated by the black arrows. To observe the sigma phase more clearly, SEM-BSE observations were conducted in the H650-15 HEA. The observation results in Fig. 3 show that submicron sigma-phase particles are distributed on the grain boundaries of the recrystallized regions. This is consistent with a previous study in which sigma phase particles were found to be <2% and were distributed near recrystallized regions after annealing of a NiFeCoCrMn cold-rolled sheet at

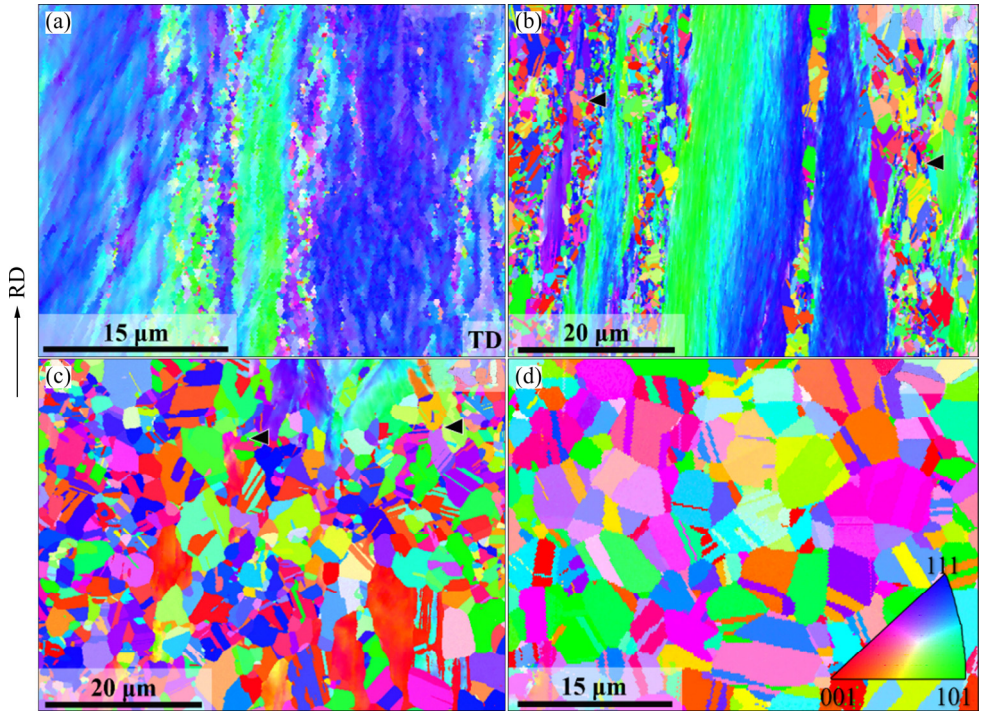


**Fig. 2** EBSD inverse pole figure (IPF) maps of as-rolled (a), H650-10 (b), H650-15 (c) and H800-10 (d) samples of NiFeCoCrMn HEAs

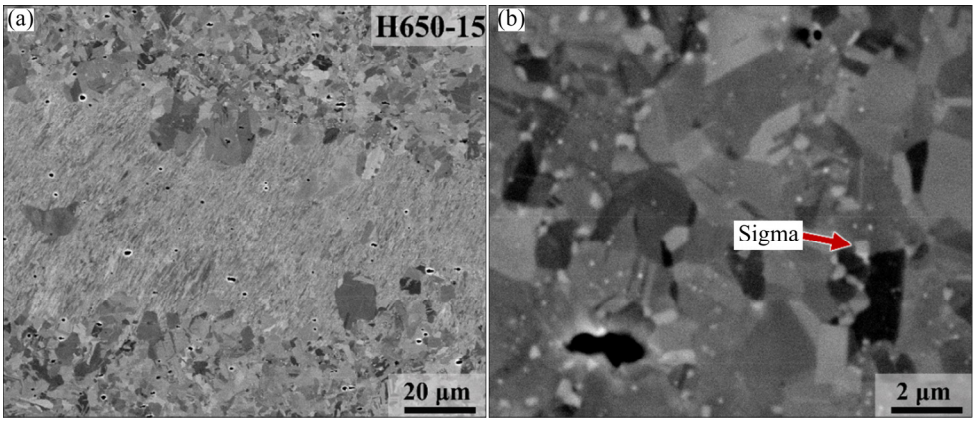


**Fig. 3** SEM-BSE microstructure of H650-10 HEA (a) and zoom-in image of recrystallized region showing sigma-phase particles distributed on grain boundaries (b)

650 °C for 1 h [22]. In the sample annealed at 800 °C for 10 min, the IPF map clearly reveals fully recrystallized microstructures composed of equiaxed grains of ~3.2 μm with abundant annealing twins.

### 3.2 Tensile properties

Engineering stress–engineering strain curves for the four studied HEAs are depicted in Fig. 4(a). The yield strength ($\sigma_y$), ultimate tensile strength ($\sigma_u$), uniform elongation ($\varepsilon_u$) and elongation to fracture ($\varepsilon_f$) of these HEAs are listed in Table 1. It is known that $\varepsilon_f$ is composed of uniform and non-uniform elongation components (starting from necking to fracture). In as much as a significant proportion of the plastic deformation at fracture is confined to the neck region, $\varepsilon_f$ depends on the specimen gauge length. To show the plastic deformation ability of the NiFeCoCrMn HEA at different states clearly, both uniform elongation and elongation to fracture are listed here. The flow stress of the as-rolled HEA reaches ~1256 MPa immediately after elastic deformation and then decreased without obvious strain hardening and uniform elongation. Note that although its $\varepsilon_f$-value is perceptible, the $\varepsilon_u$-value is negligible. This is consistent with other research,

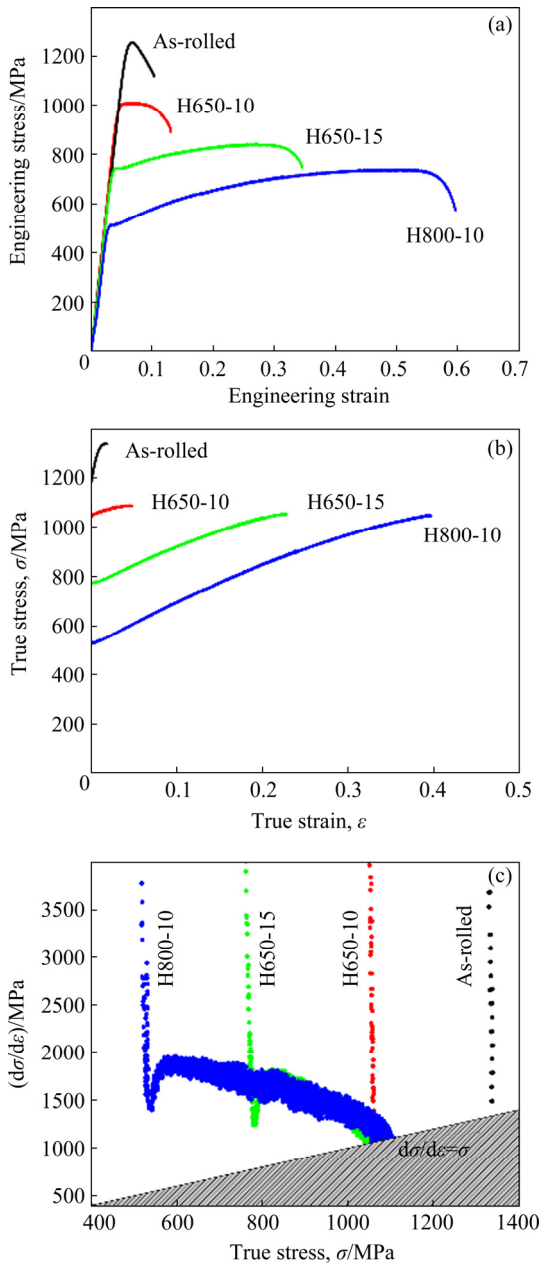


**Fig. 4** Engineering stress–engineering strain curves (a), true stress–true strain curves (b) and work hardening rate (derivative of true stress–true strain curves, $d\sigma/d\varepsilon$) plotted as function of true stress (c), for as-rolled and annealed NiFeCoCrMn HEAs (The grey area in (c) shows the necking region according to Considere's criterion)

e.g., a Ti−15Mo−1Fe alloy showed local deformation soon after yielding (i.e., no significant uniform elongation), even with a total elongation of 20% [38] and, after subsequent annealing, both $\sigma_y$ and $\sigma_u$ decreased, accompanied by elongation recovery at an increased annealing temperature and/or prolonged duration. The $\sigma_y$ of Sample H650-10 remains very high slightly over 1 GPa, while $\varepsilon_u$ recovers to ~4%. By increasing the duration to 15 min at 650 °C, $\sigma_y$-value decreases to ~742 MPa while $\varepsilon_u$ increases to a considerable value of ~24%. Ulteriorly, after full recrystallization at 800 °C for 10 min, the $\sigma_y$-value reduces to ~511 MPa but $\varepsilon_u$ increases significantly up to ~49%. The true stress–true strain curves in Fig. 4(b) are calculated from the corresponding engineering stress–engineering strain curves in Fig. 4(a) up to the point at which geometric instabilities start to form. Based on these curves, the derivatives ($d\sigma/d\varepsilon$) are plotted as a function of the true stress $\sigma$, as shown in Fig. 4(c). The grey area indicates the region in which necking is predicted to occur according to Considere's criterion. The strain hardening rates of the as-rolled and H650-10 samples drop steeply to reach the instability values with a small stress increment due to the lack of dislocation accumulation by recrystallized grains [39−41]. However, with increase in $f_{rec}$ to 74% and 100%, the strain hardening rate shows conspicuous prolonged stages, which predicts higher strains for the onset of necking.

**Table 1** Recrystallized fraction ($f_{rec}$), average size of recrystallized grains ($d_{rec}$) and tensile properties of as-rolled and annealed NiFeCoCrMn alloys

| Sample | $f_{rec}$/% | $d_{rec}$/μm | $\sigma_y$/MPa | $\sigma_u$/MPa | $\varepsilon_f$/% | $\varepsilon_u$/% |
|---|---|---|---|---|---|---|
| As-rolled | 0 | − | 1188 | 1256 | 4 | − |
| H650-10 | 37 | 0.8 | 1003 | 1010 | 9 | 4 |
| H650-15 | 74 | 1.1 | 742 | 840 | 31 | 24 |
| H800-10 | 100 | 2.5 | 511 | 738 | 57 | 49 |

### 3.3 Fractography

Representative fracture surfaces of NiFeCoCrMn HEAs with different recrystallized fractions are shown in Fig. 5. The fracture surface of the as-rolled HEA exhibits nonuniformly-sized coarse dimples, which are likely to be originated from inclusions. The fractography seems different from that of the cleavage feature in brittle alloys, which can probably be ascribed to a certain amount of strain in the necking region before failure, with deformation occurring mainly in the subgrains. Dimples are also observed on the tensile fracture surface of the NiFeCoCrMn HEA sample treated by high-pressure torsion prior to tensile testing, which appears rather brittle [42]. Further study is needed

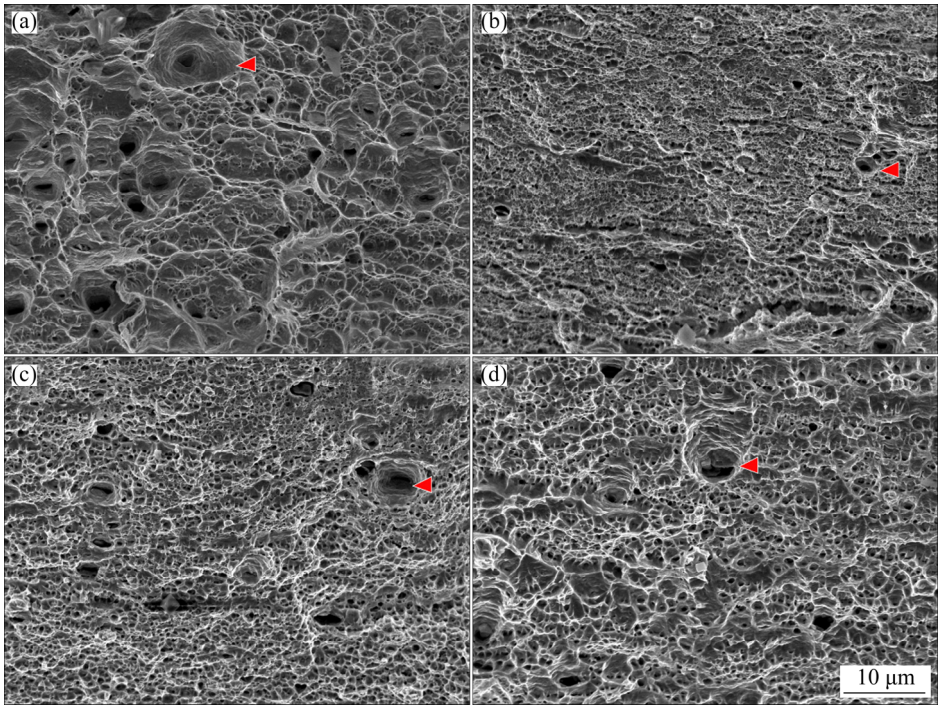


**Fig. 5** Morphologies of fracture surfaces of as-rolled (a), H650-10 (b), H650-15 (c) and H800-10 (d) specimens of NiFeCoCrMn HEAs

to clarify the specific fracture mechanism of the as-rolled sample. After the formation of equiaxed grains by recrystallization, ductile dimples are clearly present, with some large ones surrounded by small ones. Some of these dimples (especially the large ones) are also likely to be originated from inclusion sites, which is a common phenomenon in metals [43,44]. The inclusions in the present samples are mainly oxides, as indicated by the EDX spectra. The presence of such inclusions has been previously observed in this alloy [45], which is probably the result of reactions between the constituent elements and the impurities introduced through the raw materials and melting. It is considered that the considerably larger dimples are initiated at the remaining inclusions, as they are found in very pure materials elongated to fracture [42]. The average dimple size in the recrystallized samples increases with the increase in the recrystallized fraction and is accompanied by an increase in the mean size of the recrystallized grains. Also, the increase in average dimple size is consistent with the improved ductility (Fig. 4). These phenomena have been observed before [46].

### 3.4 Discussion

Dislocations can become greatly accumulated after cold work, which produces strengthening by hindering the movement of other dislocations. In the current NiFeCoCrMn HEA with a low stacking fault energy, deformation twins can also be induced by cold work [22]. The presence of the deformation twins is due to the fact that the critical resolved shear stress required for twinning onset is attained at certain strains during cold work [36]. After subsequent annealing, recrystallization occurs; i.e., a new set of strain-free and equiaxed grains are formed, the extent of which depends on both temperature and duration. In the current case, the $f_{rec}$ is adjusted to ~37%, 74% and 100% in H650-10, H650-15 and H800-10 samples, respectively. The different tailored microstructures determine their resultant mechanical properties.

Here, the possible strengthening mechanisms in the investigated HEAs include grain boundary strengthening ($\Delta\sigma_{gb}$), dislocation strengthening ($\Delta\sigma_{dis}$) and precipitation strengthening ($\Delta\sigma_{p}$), which can be expressed as

$$\sigma_y=\sigma_A+\Delta\sigma_{gb}+\Delta\sigma_{dis}+\sigma_p \quad (1)$$

where $\sigma_A$ is the lattice friction stress (125 MPa for NiFeCoCrMn HEA [47]). In general, precipitation strengthening occurs by either dislocation shearing or the Orowan dislocation bypass mechanism. The shearing mechanism is active for coherent precipitates with small radius, whereas the Orowan

bypass mechanism occurs when the precipitates are relatively large or incoherent. Sigma phase with tetragonal structure has been found to be incoherent with the FCC matrix, not only due to their structural difference but also their lattice parameter difference [48]. Therefore, the Orowan mechanism plays a role in strengthening.

When precipitates are bypassed through the Orowan dislocation looping mechanism, the increment in yield strength, $\Delta\sigma_{or}$, can be expressed as [49]

$$\Delta\sigma_{or}=M\frac{0.4Gb}{\pi\sqrt{1-\upsilon}}\frac{\ln(2\bar{r}/b)}{\lambda} \tag{2}$$

where $M$(=3.06) is the Taylor factor for poly-crystalline FCC materials [50], $G$ is the shear modulus of the matrix, 80 GPa [51], $b$ is the magnitude of the Burgers vector of the matrix, 0.255 nm, $\upsilon$ is Poisson's ratio of the matrix, 0.26 [51], $\bar{r}(=\sqrt{2/3}r)$ is the mean radius of a circular cross section in a random plane for a spherical precipitate, $r$ is the mean precipitate radius, and $\lambda$ is the edge-to-edge inter-precipitate spacing. Here, $r$ is approximate to be 125 nm, with a similar range to previous studies [23,52]. Assuming that spherical precipitates are distributed on a cubic grid, which is valid simplification for a small volume fraction of precipitates, then $\lambda=2\bar{r}(\sqrt{\pi/(4f)}-1)$, where $f$ is the volume fraction of precipitates, about 0.4% determined by the EBSD analysis. By inserting data into the equation, the increment of yield strength due to sigma-phase precipitates is about 23 MPa. As expected, the precipitation strengthening is very week and could be neglected.

Dislocation strengthening is attributed to the interaction between dislocations, which is closely linked with the dislocation density, as described by the Bailey−Hirsch formula [53]. In the completely recrystallized state, the dislocation density is considered to be very low compared with that in the severely deformed state [54]. The dislocation density can be roughly estimated by the Williamson−Hall method [55,56], which is widely used to evaluate the effects of lattice strain ($\varepsilon_{str}$) and grain size ($d$). For FCC materials, the dislocation density ($\rho$) is derived as follows [57]:

$$\rho=16.1\varepsilon_{str}^2/b^2 \tag{3}$$

The crystallite size and lattice strain, which are two main sources contributing to peak broadening ($\Delta\beta_{hkl}$), can be calculated by Williamson−Hall equation [58]:

$$\Delta\beta_{hkl}=\beta_S-\beta_{inst}=\beta_{size}+\beta_{strain} \tag{4}$$

$$\Delta\beta\cos\theta=\lambda/d+4\varepsilon_{str}\sin\theta \tag{5}$$

where $\beta_S$ is an integral breadth of Bragg peak, $\beta_{inst}$, $\beta_{size}$ and $\beta_{strain}$ are the integral breadths dependent on instrumental, grain size and strain effects, respectively. $\theta$ is the diffraction angle and $\lambda$ is the wave length of radiation used. The term ($\Delta\beta\cos\theta$), i.e., ($\beta_S-\beta_{inst}$)$\cos\theta$ can be plotted with respect to ($4\sin\theta$), and accordingly, the slope and $y$-intersect of the fitted line represent lattice strain ($\varepsilon_{str}$) and grain size ($d$), respectively.

Considering that the crystallite size is >100 nm, the term ($\beta_{size}$) should be ignored [59]. Inserting the fitted values into Eq. (3) shows that the dislocation densities of the as-rolled and H800-10 HEAs are $3.82\times10^{13}$ m$^{-2}$ and $1.47\times10^{12}$ m$^{-2}$, respectively. The dislocation density of the as-rolled sample is an order of magnitude larger than that of the recrystallized sample, which is consistent with the previous estimation [60]. It can be concluded that dislocation hardening results from the deformed microstructure containing high-density dislocations.

In the view of the duplex microstructures of the partially recrystallized HEAs, it can be simply assumed that the yield strength is proportional to $f_{rec}$ [22]:

$$\sigma_y=\sigma_A+f_{rec}\Delta\sigma_{rec}+(1-f_{rec})\Delta\sigma_{def} \tag{6}$$

where $\Delta\sigma_{def}$ is the $\sigma_y$ increment of the cold-rolled samples and $\Delta\sigma_{rec}$ is the $\sigma_y$ increment of the recrystallized samples, which is attributed to $\Delta\sigma_{gb}$ being mainly based on the Hall−Petch relationship. The strengthening coefficient ($k$) in the Hall−Petch relationship ($\sigma=\sigma_0+kd^{-1/2}$) was calculated to be 494 MPa/m$^{1/2}$ [47]. Assuming that the deformed microstructures are unchanged during annealing, the $\Delta\sigma_{gb}$ values based on the Hall−Petch relationship are somewhat higher than those calculated by Eq. (2) for the H650-10 and H650-15 HEAs. This is probably because the residual unrecrystallized deformed microstructures are recovered, even though they are not fully recrystallized during heating, while the interior dislocation density is reduced by a certain degree. The recovery of ductility attributed to recrystallized equiaxed grains with a certain $f_{rec}$ is significant for the integrated performance of HEAs. Thus, through

microstructural adjustment by means of partial recrystallization, a trade-off between strength and ductility can be obtained.

## 4 Conclusions

(1) The microstructure of the sample annealed at 650 °C for 10 min is composed of recrystallized equiaxed grains with a recrystallized fraction of ~37%. It is significantly increased to ~74% by prolonging the duration to 15 min. Full recrystallization in sheets can be attained by annealing at 800 °C for ≥10 min.

(2) Partially recrystallized microstructures composed of elongated deformed grains and strain-free equiaxed grains with a negligible fraction of sigma phase are obtained by annealing the sheets at 650 °C.

(3) With increase in the recrystallized fraction, the yield strength decreases, accompanied by increased ductility. The strengthening is due to the unrecrystallized grains remaining a high density of dislocations, whereas the ductility benefits from the presence of recrystallized strain-free grains.

## Acknowledgments

This research was sponsored by the National Natural Science Foundation of China (Nos. 51301123, 51971099), and the open funds of State Key Laboratory of Materials Processing and Die & Mould Technology, China (No. P2019-005).

## References

[1] SENKOV O N, WILKS G B, MIRACLE D B, CHUANG C P, LIAW P K. Refractory high-entropy alloys [J]. Intermetallics, 2010, 18: 1758−1765.

[2] REN M X, LI B S, FU H Z. Formation condition of solid solution type high-entropy alloy [J]. Transactions of Nonferrous Metals Society of China, 2013, 23: 991−995.

[3] ZHANG Y, ZUO T T, TANG Z, GAO M C, DAHMEN K A, LIAW P K, LU Z P. Microstructures and properties of high-entropy alloys [J]. Progress in Materials Science, 2014, 61: 1−93.

[4] GEORGE E P, RAABE D, RITCHIE R O. High-entropy alloys [J]. Nature Reviews Materials, 2019, 4: 515−534.

[5] XU Q, CHEN D Z, WANG C R, CAO W C, WANG Q, CUI H Z, ZHANG S Y, CHEN R R. Effects of La on microstructure and mechanical properties of NbMoTiVSi0.2 refractory high entropy alloys [J]. Transactions of Nonferrous Metals Society of China, 2021, 31: 512−520.

[6] CANTOR B, CHANG I T H, KNIGHT P, VINCENT A J B. Microstructural development in equiatomic multicomponent alloys [J]. Materials Science and Engineering A, 2004, 375−377: 213−218.

[7] BERND G, ANTON H, DHIRAJ C, CHANG E H, GEORGE E P, RITCHIE R O. A fracture-resistant high-entropy alloy for cryogenic applications [J]. Science, 2014, 345: 1153.

[8] ZHANG Z J, MAO M M, WANG J, GLUDOVATZ B, ZHANG Z, MAO S X, GEORGE E P, YU Q, RITCHIE R O. Nanoscale origins of the damage tolerance of the high-entropy alloy CrMnFeCoNi [J]. Nature Communications, 2015, 6: 10143.

[9] LAURENT-BROCQ M, AKHATOVA A, PERRIÈRE L, CHEBINI S, SAUVAGE X, LEROY E, CHAMPION Y. Insights into the phase diagram of the CrMnFeCoNi high entropy alloy [J]. Acta Materialia, 2015, 88: 355−365.

[10] MA D, GRABOWSKI B, KÖRMANN F, NEUGEBAUER J, RAABE D. Ab initio thermodynamics of the CoCrFeMnNi high entropy alloy: Importance of entropy contributions beyond the configurational one [J]. Acta Materialia, 2015, 100: 90−97.

[11] FENG H, WANG Z, WU Q, LI J, WANG J, LIU C T. Phase separation of metastable CoCrFeNi high entropy alloy at intermediate temperatures [J]. Scripta Materialia, 2017, 126: 15−19.

[12] LAPLANCHE G, KOSTKA A, REINHART C, HUNFELD J, EGGELER G, GEORGE E P. Reasons for the superior mechanical properties of medium-entropy CrCoNi compared to high-entropy CrMnFeCoNi [J]. Acta Materialia, 2017, 128: 292−303.

[13] LU Y P, GAO X Z, JIANG L, CHEN Z N, WANG T M, JIE J C, KANG H J, ZHANG Y B, GUO S, RUAN H H, ZHAO Y H, CAO Z Q, LI T J. Directly cast bulk eutectic and near-eutectic high entropy alloys with balanced strength and ductility in a wide temperature range [J]. Acta Materialia, 2017, 124: 143−150.

[14] CHEN R R, QIN G, ZHENG H T, WANG L, SU Y Q, CHIU Y L, DING H S, GUO J J, FU H Z. Composition design of high entropy alloys using the valence electron concentration to balance strength and ductility [J]. Acta Materialia, 2018, 144: 129−137.

[15] FU J X, CAO C M, TONG W, PENG L M. Effect of thermomechanical processing on microstructure and mechanical properties of CoCrFeNiMn high entropy alloy [J]. Transactions of Nonferrous Metals Society of China, 2018, 28: 931−938.

[16] PENG J, LI Z Y, JI X B, SUN Y L, FU L M, SHAN A D. Decomposition kinetics of carbon-doped FeCoCrNiMn high-entropy alloy at intermediate temperature [J]. Transactions of Nonferrous Metals Society of China, 2020, 30: 1884−1894.

[17] HE J Y, LIU W H, WANG H, WU Y, LIU X J, NIEH T G, LU Z P. Effects of Al addition on structural evolution and tensile properties of the FeCoNiCrMn high-entropy alloy system [J]. Acta Materialia, 2014, 62: 105−113.

[18] HE J Y, WANG H, HUANG H L, XU X D, CHEN M W, WU Y, LIU X J, NIEH T G, AN K, LU Z P. A precipitation-hardened high-entropy alloy with outstanding tensile properties [J]. Acta Materialia, 2016, 102: 187−196.

[19] ZHAO Y Y, CHEN H W, LU Z P, NIEH T G. Thermal stability and coarsening of coherent particles in a precipitation-hardened (NiCoFeCr)94Ti2Al4 high-entropy alloy [J]. Acta Materialia, 2018, 147: 184−194.

[20] HE F, CHEN D, HAN B, WU Q F, WANG Z J, WEI S L, WEI D X, WANG J C, LIU C T, KAI J J. Design of D022 superlattice with superior strengthening effect in high entropy alloys [J]. Acta Materialia, 2019, 167: 275−286.

[21] XU J, CAO C M, GU P, PENG L M. Microstructures, tensile properties and serrated flow of $Al_x$CrMnFeCoNi high entropy alloys [J]. Transactions of Nonferrous Metals Society of China, 2020, 30: 746−755.

[22] BAE J W, MOON J, MIN J J, YIM D, KIM D, LEE S, KIM H S. Trade-off between tensile property and formability by partial recrystallization of CrMnFeCoNi high-entropy alloy [J]. Materials Science and Engineering A, 2017: 703.

[23] STEPANOV N D, SHAYSULTANOV D G, OZEROV M S, ZHEREBTSOV S V, SALISHCHEV G A. Second phase formation in the CoCrFeNiMn high entropy alloy after recrystallization annealing [J]. Materials Letters, 2016, 185: 1−4.

[24] SUN S J, TIAN Y Z, LIN H R, YANG H J, DONG X G, WANG Y H, ZHANG Z F. Achieving high ductility in the 1.7 GPa grade CoCrFeMnNi high-entropy alloy at 77 K [J]. Materials Science and Engineering A, 2019, 740−741: 336−341.

[25] KLIMOVA M V, SHAYSULTANOV D G, ZHEREBTSOV S V, STEPANOV N D. Effect of second phase particles on mechanical properties and grain growth in a CoCrFeMnNi high entropy alloy [J]. Materials Science and Engineering A, 2019, 748: 228−235.

[26] WU S W, WANG G, WANG Q, JIA Y D, YI J, ZHAI Q J, LIU J B, SUN B A, CHU H J, SHEN J, LIAW P K, LIU C T, ZHANG T Y. Enhancement of strength-ductility trade-off in a high-entropy alloy through a heterogeneous structure [J]. Acta Materialia, 2019, 165: 444−458.

[27] WU S W, XU L, MA X D, JIA Y F, MU Y K, JIA Y D, WANG G, LIU C T. Effect of annealing temperatures on microstructure and deformation behavior of Al0.1CrFeCoNi high-entropy alloy [J]. Materials Science and Engineering A, 2021, 805: 140523.

[28] KLIMOVA M, SHAYSULTANOV D, SEMENYUK A, ZHEREBTSOV S, STEPANOV N. Effect of carbon on recrystallised microstructures and properties of CoCrFeMnNi-type high-entropy alloys [J]. Journal of Alloys & Compounds, 2021, 851: 156839.

[29] GAO N, LU D H, ZHAO Y Y, LIU X W, LIU G H, WU Y, LIU G, FAN Z T, LU Z P, GEORGE E P. Strengthening of a CrMnFeCoNi high-entropy alloy by carbide precipitation [J]. Journal of Alloys and Compounds, 2019, 792: 1028−1035.

[30] LIU G, LU D H, LIU X W, LIU F C, YANG Q, DU H, HU Q, FAN Z T. Solute segregation effect on grain boundary migration and Hall–Petch relationship in CrMnFeCoNi high-entropy alloy [J]. Materials Science and Technology, 2019, 35: 1−9.

[31] DZIASZYK S, PAYTON E J, FRIEDEL F, MARX V, EGGELER G. On the characterization of recrystallized fraction using electron backscatter diffraction: A direct comparison to local hardness in an IF steel using nanoindentation [J]. Materials Science and Engineering A, 2010, 527: 7854−7864.

[32] LAPLANCHE G, GADAUD P, HORST O, OTTO F, EGGELER G, GEORGE E P. Temperature dependencies of the elastic moduli and thermal expansion coefficient of an equiatomic, single-phase CoCrFeMnNi high-entropy alloy [J]. Journal of Alloys & Compounds, 2015, 623: 348−353.

[33] DEY S, GAYATHRI N, BHATTACHARYA M, MUKHERJEE P. In situ XRD studies of the process dynamics during annealing in cold-rolled copper [J]. Metallurgical and Materials Transactions A, 2016, 47: 6281−6291.

[34] GUPTA T R, SIDHU S S, KATIYAR J K, PAYAL H S. Measurements of lattice strain in cold-rolled CR4 steel sheets using X-ray diffraction [J]. Materials Science and Engineering B, 2021, 264: 114930.

[35] JO Y H, JUNG S, CHOI W M, SOHN S S, KIM H S, LEE B J, KIM N J, LEE S. Cryogenic strength improvement by utilizing room-temperature deformation twinning in a partially recrystallized VCrMnFeCoNi high-entropy alloy [J]. Nature Communications, 2017, 8: 15719.

[36] LAPLANCHE G, KOSTKA A, HORST O M, EGGELER G, GEORGE E P. Microstructure evolution and critical stress for twinning in the CrMnFeCoNi high-entropy alloy [J]. Acta Materialia, 2016, 118: 152−163.

[37] CHEN S, TSENG K K, TONG Y, LI W, TSAI C W, YEH J W, LIAW P K. Grain growth and Hall−Petch relationship in a refractory HfNbTaZrTi high-entropy alloy [J]. Journal of Alloys and Compounds, 2019, 795: 19−26.

[38] MIN X H, EMURA S, SEKIDO N, NISHIMURA T, TSUCHIYA K, TSUZAKI K. Effects of Fe addition on tensile deformation mode and crevice corrosion resistance in Ti−15Mo alloy [J]. Materials Science and Engineering A, 2010, 527: 2693−2701.

[39] HE X, LIU L, ZENG T, YAO Y. Micromechanical modeling of work hardening for coupling microstructure evolution, dynamic recovery and recrystallization: Application to high entropy alloys [J]. International Journal of Mechanical Sciences, 2020, 177: 105567.

[40] CHEN F, CUI Z S, CHEN S J. Recrystallization of 30Cr2Ni4MoV ultra-super-critical rotor steel during hot deformation. Part I: Dynamic recrystallization [J]. Materials Science and Engineering A, 2011, 528: 5073−5080.

[41] SHABANI A, TOROGHINEJAD M R. Evaluation of microstructure and texture formation during annealing of cold-rolled FeCrCuMnNi multiphase high-entropy alloy [J]. Transactions of Nonferrous Metals Society of China, 2020, 30: 449−462.

[42] SCHUH B, MENDEZ-MARTIN F, VÖLKER B, GEORGE E P, CLEMENS H, PIPPAN R, HOHENWARTER A. Mechanical properties, microstructure and thermal stability of a nanocrystalline CoCrFeMnNi high-entropy alloy after severe plastic deformation [J]. Acta Materialia, 2015, 96: 258−268.

[43] RIZAL S, HOMMA H, NAZER M, KISHIDA E. Experimental approach to dimple fracture mechanisms under short pulse loading [J]. Engineering Fracture Mechanics, 2002, 69: 1377−1390.

[44] ZHU C Y, WU H, ZHU H G, LI X D, TU C L, XIE Z H. Mechanical properties and fracture mechanism of as-cast MnFeCoCuNi$_x$ high-entropy alloys [J]. Transactions of Nonferrous Metals Society of China, 2021, 31: 222−231.

[45] OTTO F, DLOUHÝ A, PRADEEP K G, KUBĚNOVÁ M, RAABE D, EGGELER G, GEORGE E P. Decomposition of the single-phase high-entropy alloy CrMnFeCoNi after prolonged anneals at intermediate temperatures [J]. Acta Materialia, 2016, 112: 40−52.

[46] AAL M I A E, UM H Y, YOON E Y, KIM H S. Microstructure evolution and mechanical properties of pure aluminum deformed by equal channel angular pressing and direct extrusion in one step through an integrated die [J]. Materials Science and Engineering A, 2015, 625: 252−263.
[47] OTTO F, DLOUHÝ A, SOMSEN C, BEI H, EGGELER G, GEORGE E P. The influences of temperature and microstructure on the tensile properties of a CoCrFeMnNi high-entropy alloy [J]. Acta Materialia, 2013, 61: 5743−5755.
[48] ZHANG L, HUO X F, WANG A G, DU X H, ZHANG L, LI W P, ZOU N F, WAN G, DUAN G S, WU B L. A ductile high entropy alloy strengthened by nano sigma phase [J]. Intermetallics, 2020: 122.
[49] WEN H, TOPPING T D, ISHEIM D, SEIDMAN D N, LAVERNIA E J. Strengthening mechanisms in a high-strength bulk nanostructured Cu−Zn−Al alloy processed via cryomilling and spark plasma sintering [J]. Acta Materialia, 2013, 61: 2769−2782.
[50] ZEHETBAUER M, SEUMER V. Cold work hardening in stages IV and V of F.C.C. metals—I. Experiments and interpretation [J]. Acta Metallurgica et Materialia, 1993, 41: 577−588.
[51] WU Z, BEI H, PHARR G M, GEORGE E P. Temperature dependence of the mechanical properties of equiatomic solid solution alloys with face-centered cubic crystal structures [J]. Acta Materialia, 2014, 81: 428−441.
[52] LEE U, STRAUMAL B, PARK N. Dynamic precipitation of $\sigma$-phase and element partitioning in equiatomic CoCrFeMnNi high-entropy alloy [J]. Materials Science and Engineering A, 2021: 804.
[53] BAILEY J E, HIRSCH P B. The recrystallization process in some polycrystalline metals [J]. Procroysocsera, 1962, 267: 11−30.
[54] TWISS R J. Theory and applicability of a recrystallized grain size paleopiezometer [J]. Pure & Applied Geophysics, 1977, 115: 227−244.
[55] THIRATHIPVIWAT P, SONG G, BEDNARCIK J, KÜHN U, GEMMING T, NIELSCH K, HAN J. Compositional complexity dependence of dislocation density and mechanical properties in high entropy alloy systems [J]. Progress in Natural Science: Materials International, 2020, 30: 545−551.
[56] YOGAMALAR R, SRINIVASAN R, VINU A, ARIGA K, BOSE A C. X-ray peak broadening analysis in ZnO nanoparticles [J]. Solid State Communications, 2009, 149: 1919−1923.
[57] SMALLMAN G K W R E. III. Dislocation densities in some annealed and cold-worked metals from measurements on the X-ray Debye-Scherrer spectrum [J]. Philosophical Magazine, 1956, 1: 34−46.
[58] HALL G K W W H. X-ray line broadening from filed aluminium and wolfram [J]. Acta Metallurgica, 1953, 1: 22−31.
[59] KRIL C E, BIRRINGER R. Estimating grain-size distributions in nanocrystalline materials from X-ray diffraction profile analysis [J]. Philosophical Magazine A, 1998, 77: 621−640.
[60] STEPANOV N, TIKHONOVSKY M, YURCHENKO N, ZYABKIN D, KLIMOVA M, ZHEREBTSOV S, EFIMOV A, SALISHCHEV G. Effect of cryo-deformation on structure and properties of CoCrFeNiMn high-entropy alloy [J]. Intermetallics, 2015, 59: 8−17.

# 部分再结晶对 NiFeCoCrMn 高熵合金显微组织和拉伸性能的影响

杜 辉[1,2,3,4]，蔡嘉洪[1,2]，王亚松[4]，姚俊卿[4]，陈 强[5]，崔 宇[1,2]，刘鑫旺[4]

1. 武汉科技大学 冶金装备及其控制教育部重点实验室，武汉 430081；
2. 武汉科技大学 机械传动与制造工程湖北省重点实验室，武汉 430081；
3. 武汉科技大学 精密制造研究院，武汉 430081；
4. 华中科技大学 材料科学与工程学院 材料成形与模具技术国家重点实验室，武汉 430074；
5. 西南技术工程研究所，重庆 400039

**摘 要**：为了调控 NiFeCoCrMn 高熵合金强度和塑性之间的平衡关系，采用传统的热力学加工技术(冷轧和再结晶)，通过不同的再结晶退火工艺得到不同程度的位错强化，并对具有不同再结晶比例的合金进行拉伸性能测试。随着再结晶比例的增加，即应变硬化程度的下降，合金的均匀伸长率和加工硬化率显著提高，但屈服强度和抗拉强度降低。尤其在 650 ℃分别退火 10 min 和 15 min 时，获得的再结晶比例分别为 37%和 74%，相应的屈服强度为 1003 MPa 和 742 MPa，均匀伸长率为 4%和 24%。强化主要来源于含高密度位错的未再结晶组织，而塑性则是由无应变的再结晶晶粒产生。

**关键词**：高熵合金；部分再结晶；显微组织；拉伸性能；强化机制

**(Edited by Bing YANG)**